Antiferromagnetic bipolar semiconductor LaMnPO with ZrCuSiAs-type structure

Hiroshi Yanagi,[1,a)] Takumi Watanabe,[1] Katsuaki Kodama,[2] Satoshi Iikubo,[2,b)] Shin-ichi Shamoto,[2] Toshio Kamiya,[1,3] Masahiro Hirano,[3,4] and Hideo Hosono[1,3,4]
[1]*Materials and Structures Laboratory, Tokyo Institute of Technology, 4259 Nagatsuta, Midori-ku, Yokohama 226-8530, Japan*
[2]*Japan Atomic Energy Agency (JAEA), 2-4 Shirane Shirakata, Tokai-mura, Naka-gun, Ibaraki 319-1195, Japan*
[3]*ERATO-SORST, JST, in Frontier Research Center, Tokyo Institute of Technology, 4259 Nagatsuta, Midori-ku, Yokohama 226-8530, Japan*
[4]*Frontier Research Center, Tokyo Institute of Technology, 4259 Nagatsuta, Midori-ku, Yokohama 226-8530, Japan*

(Received 30 January 2009; accepted 26 March 2009; published online 7 May 2009)

Electronic and magnetic properties of a layered compound LaMnPO are examined in relation to a newly discovered iso-structural superconductor LaFeAs(P)O. Neutron diffraction measurements, together with temperature dependent magnetic susceptibility, clarify that LaMnPO is an antiferromagnet at least up to 375 K. The spin moment of a Mn ion is determined to be 2.26 μ_B at room temperature, and the spin configuration is antiparallel in the Mn–P plane and parallel between the Mn–P planes, which is rather different from that of LaFeAsO. Optical absorption spectra, photoemission spectra, and temperature dependent electrical conductivity indicate that LaMnPO is a semiconductor. Furthermore, nominally undoped LaMnPO exhibits *n*-type conduction while the conduction type is changed by doping of Cu or Ca to the La sites, indicating that LaMnPO is a bipolar conductor. Density functional calculation using the GGA+U approximation supports the above conclusions; the electronic band structure has an open band gap and the antiferromagnetic spin configuration is more stable than the ferromagnetic one. © *2009 American Institute of Physics*.
[DOI: 10.1063/1.3124582]

I. INTRODUCTION

Layered transition-metal compounds have been studied intensively as correlated electron systems originating from the 3*d* electrons in the transition metal ions. Their distinct electronic and magnetic properties invoke unconventional functions such as high transition temperature (high-T_c) superconductivity,[1] tunneling magnetoresistance,[2] and large thermoelectric power.[3] Our group has studied mixed anion layered compounds containing transition metals, which include a *LnMX*O system (*Ln*=lanthanoid; *M*=Fe, Co, Ni; *X*=P, As) with the ZrCuSiAs-type crystal structure. Electronic transport and magnetic properties of the mixed anion layered compounds vary in a wide range by changing the combination of the transition metal and the anions even if the same crystal structure is maintained. Since the crystal structure of *LnMX*O is composed of alternate stacks of *Ln*-O and *M*-*X* layers as shown in Fig. 1, the chemical composition is expressed as (*Ln*O)(*MX*) in a structural formula. First-principles calculations have revealed that the 3*d* electrons in *LnMX*O are concentrated in the *M*-*X* layer and form the Fermi level,[4–6] which are thought to be related closely to the appearance of high-T_c superconductivity in electron-doped LaFeAsO and related compounds.

Actually, we have reported that electronic transport and magnetic properties of La*MX*O change largely with the transition metal element. For example, LaFePO and LaNiPO, whose transition metal ions (nominally Fe^{2+} and Ni^{2+}) have even numbers of 3*d* electrons (six for Fe^{2+} and eight for Ni^{2+}), undergo superconducting transitions.[7,8] Undoped LaFeAsO is a poor metal with an antiferromagnetic (AFM) spin configuration at the ground state. While, electron doping induces superconductivity at $T_c \sim 26$ K,[9] which is further enhanced up to ~55 K by an external pressure[10] or replacing La with other lanthanide ions (chemical pressure).[11–15] These findings triggered the new fever in high-T_c superconductor research. On the other hand, the magnetic moments of LaCo*X*O (seven 3*d* electrons for Co^{2+}) do not vanish completely, leading to an itinerant ferromagnetic (FM) phase at <43 K for LaCoPO.[16] Further, LaZn*X*O exhibit a nonmagnetic semiconductive behavior due to the closed shell $(3d)^{10}$ configuration of the Zn^{2+} ion.[17,18]

The Mn compound LaMnPO is also of great interest because Mn^{2+} has an odd number of 3*d* electrons and is expected to form a spin configuration different from those of the other La*MX*O compounds because many Mn^{2+} compounds have a half-filled pseudoclosed shell configuration $(3d_{up})^5$. In addition, investigation of LaMnPO is considered to provide complementary information to understand the electron correlation of 3*d* electrons in these layered compounds and further the superconducting mechanism in LaFe*X*O and LaNi*X*O.

[a)]Author to whom correspondence should be addressed. Electronic mail: yanagi@lucid.msl.titech.ac.jp.
[b)]Present address: WPI Advanced Institute for Materials Research Tohoku University, 2-1-1 Katahira Aoba-ku Sendai, 980-8577, Japan.

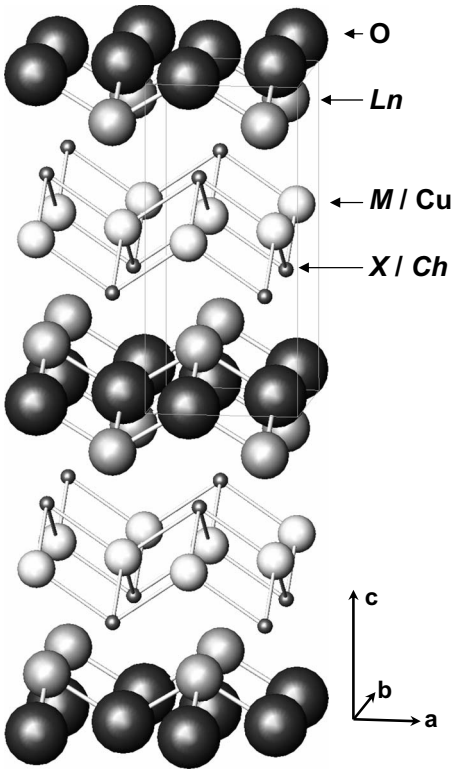

FIG. 1. Crystal structure of *LnMX*O (*Ln*=lanthanoid; *M*=Mn, Fe, Co, Ni, Zn; *X*=P. As) and LaCu*Ch*O (*Ch*=S, Se, Te), which have layered crystal structures composed of *Ln*-O and *M*-*X*/Cu-*Ch* layers.

In this paper, we measured electronic transport, optical properties, and magnetization properties of LaMnPO with single-phase polycrystalline samples. Further the magnetic structure and the electronic structure around the Fermi level were examined by neutron diffraction and synchrotron x-ray photoemission spectroscopy, respectively. We also performed density functional theory (DFT) calculations using the GGA+U approximation to know the stable crystal structure and the spin configuration along with the electronic band structure. These results show LaMnPO is an indirect transition-type semiconductor with an AFM spin configuration at room temperature. It is also found that undoped sample exhibits *n*-type conduction, which is converted to *p*-type by hole doping.

II. EXPERIMENTAL AND CALCULATIONS

The single-phase polycrystalline samples were obtained through a two-step solid-state reaction process using La (Shin-etsu Chemical, purity 99.5%), P (Rare Metallic, 99.9999%), and MnO (Soekawa Chemical, 99.9%) as starting materials. This process is different from that reported by Nientiedt *et al.*[19] In the first step of the synthesis, single-phase LaP was prepared by heating a mixture of powdered La and P with an atomic ratio of 1.00:0.97 in an evacuated silica tube at 400 °C for 12 h and then temperature was increased to 700 °C and kept for 6 h; this was because the resulting LaMnPO samples synthesized with stoichiometric LaP (La:P=1:1) contained an impurity phase of MnP. Then, a mixture of the LaP and the MnO was pressed into a pellet and heated at 1000 °C for 12 h in an evacuated silica tube. It was confirmed that the residual MnP contents in the samples were below the detection limits of our high-power x-ray diffraction (XRD) equipment (detection limit $<0.1\%$ [8,20,21]) and magnetic measurements ($<0.1\%$). Ca_3P_2 and CuO were added to the starting materials in the second step to form doped LaMnPO samples, $La_{1-x}Ca_xMnPO$, and $LaMn_{1-x}Cu_xPO$, respectively.[22]

The prepared samples were characterized by a high-power XRD (D8 ADVANCE-TXS, Bruker AXS) with Cu Kα radiation at 24 °C. Rietveld analyses were carried out using the code TOPAS3 (Ref. 23) to refine crystallographic parameters of LaMnPO. Neutron diffraction experiments were performed using a high-resolution powder diffractometer installed at JRR-3 of the Japan Atomic Energy Agency (JAEA). The collimations were open (the effective value was 35′)-open-40′-6′ and the neutron wavelength λ was 0.182 33 nm. The data were collected at room temperature (RT). Neutron Rietveld analyses were carried out using the code RIETAN-2000.[24]

Diffuse reflectance spectra were measured on fine-powdered undoped LaMnPO samples. Optical absorption spectra were taken on 150 nm thick (001) oriented epitaxial LaMnPO films on MgO (001) single-crystal substrates prepared by pulsed laser deposition in order to evaluate the optical band gap. Details in the film deposition procedure will be reported elsewhere.[25]

The electrical conductivities of the sintered pellets were measured in the temperature range 1.8–305 K with a four-probe technique (PPMS, Quantum Design). Ohmic electrodes were formed using sputtered Au films. The magnetic susceptibility were measured with a vibrating sample magnetometer (PPMS, Quantum Design) from 2.5 to 375 K under a magnetic field of 5000 Oe in a zero field cooling procedure.

Resonant photoemission spectroscopy (RPES) measurements were performed with several excitation photon energies from 636 to 639 eV, which correspond to the energy at the Mn L_3 absorption edge, in the BL23SU beam line at the Japan Synchrotron Radiation Research Institute (SPring-8). The energy resolution estimated from the Fermi edge broadening of a gold reference was ~130 meV. To prevent a charging effect, Ca-doped *p*-type conductive LaMnPO was employed for the measurements. Before the measurement, polycrystalline samples were fractured in a vacuum preparation chamber, which is attached to the measurement chamber, to obtain clean surfaces. All the measurements were performed at 20 K in an ultrahigh vacuum of $\sim 10^{-8}$ Pa.

DFT periodic calculations were performed with the Vienna *ab initio* simulation package (Ref. 26) code using a projector augmented plane wave method[27,28] and PBE96 generalized gradient approximation (GGA) functionals. Crystal structure parameters obtained by the XRD Rietveld analyses were employed as initial values, and then the lattice parameters and internal ionic coordinates were optimized so as to take the minimum total energy. Two different spin configurations were examined; one was a FM configuration where both of the two Mn ions in the unit cell were assumed to be identical, and the other was an AFM configuration where the two Mn ions were treated independently with the

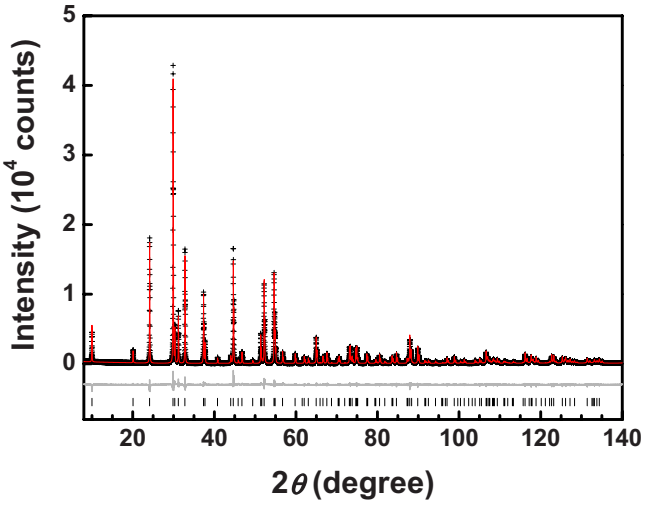

FIG. 2. (Color online) Powder XRD patterns of the LaMnPO sample and the results of the Rietveld analysis. (Upper row) Observed pattern (+) and simulated pattern obtained by the Rietveld analysis (red line). (Middle row) The difference profile between the observed and simulated patterns. (Bottom row) The positions of the Bragg reflections from LaMnPO.

spin configuration obtained by the neutron Rietveld analyses. For the latter case, self-consistent cycles converged to a total spin moment of zero, indicating an AFM configuration. GGA+U calculations were also performed because the simple GGA calculation did not reproduce the energy position of the Mn 3*d* states observed by RPES. The simplified rotationally invariant approach of Dudarev *et al.*[29] was used, where two empirical parameters, the Coulomb parameter U and the exchange parameter J, are required but appear as one independent parameter (effective Coulomb parameter) $U_{\mathrm{eff}}=U-J$, for each localized orbital. U_{eff} for Mn 3*d* electrons was varied from 0 to 6 eV, and that for La 4*f* was fixed at 11 eV.[30]

III. RESULTS AND DISCUSSION

A. Structure analyses

Figure 2 shows a powder XRD pattern for LaMnPO. All the peaks agree with those of a simulated pattern by the Rietveld analyses and no extra peak was observed, which confirms the sample was a single phase. Table I summarizes the refined structural parameters, which substantiates LaMnPO has the same crystal structure as those of La*MX*O and NdMn*X*O.[19] It belongs to the tetragonal ZrCuSiAs-type structure ($P4/nmm$), composed of alternating stacks of Mn–P and La–O layers. The Mn–P layer is built from the edge-sharing networks of MnP_4 tetrahedrons, which is distorted from the regular tetrahedron. The distortion is evaluated from deviation of the P-*M*-P bond angles from that of the regular tetrahedron (109.47°). Those for LaMnPO are 111.24° and 108.59°, whose distortions are smaller than those of LaFePO [120.2° and 104.4° (Ref. 7)], LaCoPO [127.4° and 101.3° (Ref. 31) or 121.7° and 103.7° (Ref. 16)], and LaNiPO [126.4° and 101.7° (Ref. 8)]. On the other hand, the ZnP_4 tetrahedron in LaZnPO (108.1° and 110.2° in Ref. 32 and 108.4° and 110.0° in Ref. 17) is the closest to the regular tetrahedron among the La*M*PO compounds.

TABLE I. Crystallographic parameters of LaMnPO refined by powder x-ray Rietveld analysis. The XRD data were collected at 24 °C. Occupancy and *B* values of O were fixed at 1.0 and 0.9, respectively. The reliability factor was $R_{\mathrm{wp}}=11.91\%$ and the goodness of fit parameter was $S=2.39$.

a (nm)	*c* (nm)	*V* (nm^3)
0.405786(1)	0.884341(3)	0.1456181(9)

Site	Wycoff position	*x*	*y*	*z*	*B* (Å^2)
La	2c	1/4	1/4	0.13879(4)	0.146(8)
Mn	2b	3/4	1/4	1/2	0.13(2)
O	2a	3/4	1/4	0	0.90
P	2c	1/4	1/4	0.6569(2)	0.25(3)

Figure 3(a) shows a neutron diffraction pattern (crosses), a simulated one (red line), and a difference between the observed and simulated patterns (gray line at the bottom). Table II summarizes refined structural and magnetic parameters. The obtained structural parameters agree with those obtained from the XRD measurements with the differences less than 0.5%. Figure 3(b) shows decomposition of the simulated pattern into nuclear (blue) and magnetic (red) scattering contributions. It indicates that the spin ordering information is clearly obtained from the 100 and 101 diffractions at ~25.9° and ~28.5°, respectively. The 100 diffraction disappears in the nuclear scattering due to the extinction rule originating from the *n* glide plane along the [110] direction in the space group $P4/nmm$, but is clearly observed in the magnetic scattering, indicating that the two Mn ions in the unit cell have different spin moments. Furthermore, when we assumed the direction of the magnetic moment on Mn was perpendicular to the *c*-axis, a weighted profile reliability factor, R_{wp}, became 7.18%. The value decreased to 6.18% provided that the direction was assumed to be parallel to the *c*-axis. Consequently, we concluded that the direction of the magnetic moment is parallel to the *c*-axis. The refined magnetic moment is 2.26(2) μ_B/Mn, which is much smaller than the value expected from the high-spin configuration in the localized spin scheme (5 μ_B/Mn), but much larger than that expected from the low-spin configuration (1 μ_B/Mn). The most reliable magnetic structure obtained is illustrated in Fig. 3(c), where the in-plane magnetic structure is AFM; the magnetic coupling with the nearest Mn ions, which lie in the [110] direction, is antiparallel to each other, whereas the spins couple in parallel with the second nearest Mn ions, which lie in the [100] and [010] directions. On the other hand, the interlayer spin coupling is parallel. Note that the spin configuration of LaMnPO is different from that of LaFeAsO, where the Fe spin moments are perpendicular to the *c*-axis, orders in the stripe type configuration in the Fe–As layer, and are antiparallel between the adjacent layers.[33] These results indicate that magnetic interactions among the transition metal ions in *LnMX*O are sensitive to kind of 3*d* transition metal elements (i.e., number of *d* electrons).

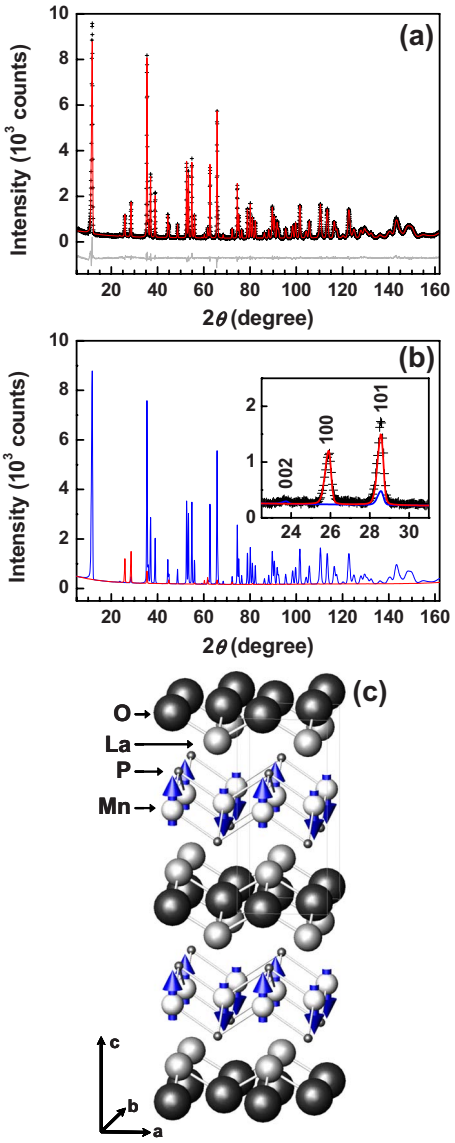

FIG. 3. (Color online) (a) Neutron powder diffraction patterns of the LaMnPO sample and the result of the Rietveld analysis. (Upper row) Observed pattern (+) and simulated pattern obtained by the Rietveld analysis (red line). (Bottom row) The difference profile between the observed and simulated patterns. (b) The simulated patterns by nuclear scattering (blue line) and magnetic scattering (red line). Inset shows a magnified view around the 100 diffraction. (c) Magnetic structure of LaMnPO.

B. Optical spectra, electrical transports, and magnetization

Optical absorption spectra were obtained from diffuse reflectance spectra by using the Kubelka–Munk relation.[34,35] To evaluate the band gap energy, two types of plots, a $[(\alpha/s)\times h\nu]^2$-$h\nu$ plot for the allowed direct transition model and a $(\alpha/s)^{1/2}$-$h\nu$ plot for the indirect transition model, where α denotes the optical absorption coefficient, $h\nu$ denotes the photon energy, and s denotes the scattering factor, are examined in Fig. 4(a). Straight lines are found in the $[(\alpha/s)\times h\nu]^2$-$h\nu$ plot in two different regions, between 1.0 and 1.5 eV and between 2.0 and 2.5 eV, which may provide direct transition gaps of ~0.9 and ~1.4 eV, respectively. On the other hand, the $(\alpha/s)^{1/2}$-$h\nu$ plot shows a straight line in a narrow photon energy region of 0.9–1.0 eV, which may give

TABLE II. Crystallographic parameters refined by powder neutron Rietveld analysis. The neutron diffraction data were collected at RT. The reliability factor was R_{wp}=6.18% and the goodness of fit parameter was S=1.32.

a (nm)			c (nm)		
0.40572(2)			0.88415(3)		
Site	x	y	z	B (Å^2)	M_{Mn} (μ_B)
La	1/4	1/4	0.1381(2)	0.52(3)	···
Mn 1	3/4	1/4	1/2	0.67(4)	2.26(2)
Mn 2	1/4	3/4	1/2	0.67(4)	−2.26(2)
O	3/4	1/4	0	0.67(4)	···
P	1/4	1/4	0.6586(2)	0.77(4)	···

an indirect band gap of ~0.9 eV. The band gap energies, obtained in this procedure, are not so confirmative because similar absorption tail structures have frequently been observed in similar compounds including LaCuChO (Ch=S, Se, Te).[36] For instance, LaCuSeO has the band gap energy of ~2.7 eV and exhibits an absorption tail extended to ~2.5 eV even in undoped samples and to ~2.0 eV in hole-doped ones, where the tails are assigned to subgap states related to defects. Therefore, we also measured optical absorption spectra using epitaxial films of LaMnPO to further examine the band gap energy. As shown in Fig. 4(b), the $(\alpha\times h\nu)^2$-$h\nu$ plot exhibits a straight line at >1.6 eV, providing a direct band gap of ~1.4 eV. On the other hand, the $\alpha^{1/2}$-$h\nu$ plot exhibits a straight line in a wide energy region

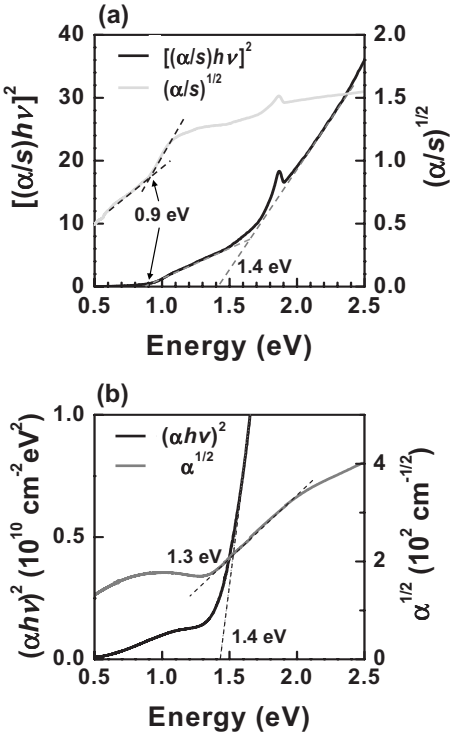

FIG. 4. (a) Absorption spectra of LaMnPO converted from diffuse reflectance spectra with the Kubelka–Munk relation. Direct band gap and indirect bad gap are estimated from the $[(\alpha/s)\times h\nu]^2$-$h\nu$ plot (black line) and the $(\alpha/s)^{1/2}$-$h\nu$ plot (gray line), respectively. (b) Optical absorption spectra of a LaMnPO epitaxial film.

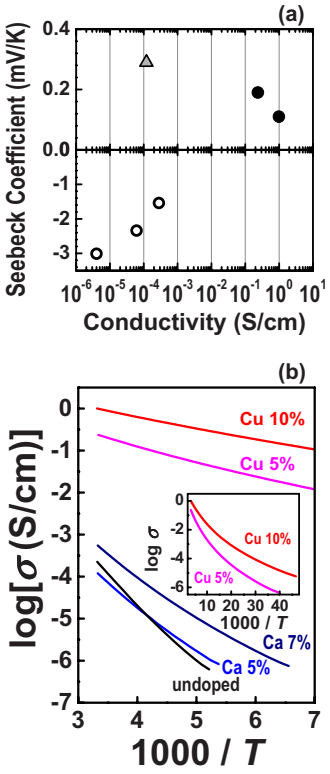

FIG. 5. (Color online) (a) Seebeck coefficients of undoped (open circles), Cu doped (closed circles), and Ca doped (triangle) LaMnPO plotted against electrical conductivity at RT. (b) (Color online) Electrical conductivities of undoped, Cu doped, and Ca doped LaMnPO as a function of temperature.

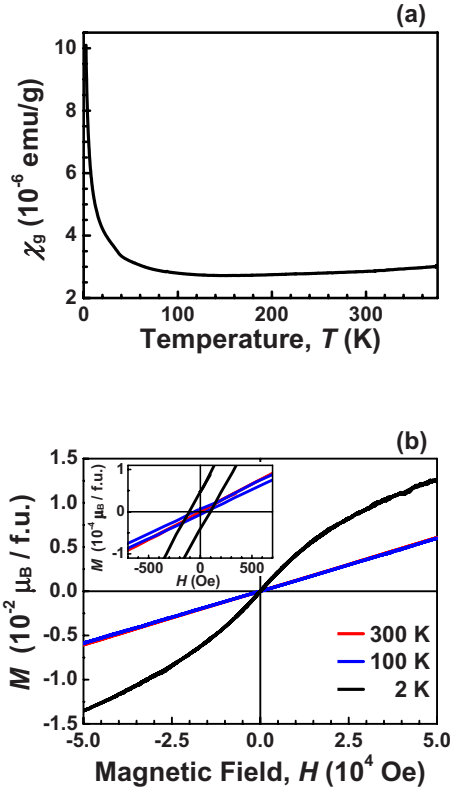

FIG. 6. (Color online) (a) Magnetic susceptibility of undoped LaMnPO as a function of temperature. (b) (Color online) Magnetization curves of undoped LaMnPO at 2, 100, and 300 K. Inset shows magnified curves in a low magnetic field region.

between 1.3–1.8 eV, although lower-energy absorption was still observed below 1.3 eV. Based on these analyses, along with the fact that the profile of the lower-energy absorption (<1.3 eV) resembles that of the subgap absorption in LaCuSeO films, we concluded that the lower-energy absorption comes from subgap states and the fundamental band gap of LaMnPO is of an indirect transition type with the band gap value of ~ 1.3 eV. These conclusions are consistent with the electronic band structure obtained by the GGA+U calculations described below.

Seebeck coefficients (S) of undoped and doped samples at RT are plotted against electrical conductivity (σ) in Fig. 5(a). All the S values in undoped samples show negative signs and the absolute S value decreases monotonically with an increase in σ, indicating that the undoped samples are n-type conductors. The S and σ values of the undoped samples scattered largely from -1 to -3 mV K^{-1} and from $\sim 10^{-6}$ to $\sim 10^{-4}$ S cm^{-1}, respectively. These scatterings are attributable to compositional deviation among the different preparation batches because similar scatterings have been observed in other family compounds such as LaZnPO.[17] The conduction carriers in the undoped LaMnPO are thought to originate in the nonstoichiometry of the synthesized samples because the chemical compositions, especially the anion ratio O:P, are difficult to control precisely in these complex compounds. On the other hand, the Ca and Cu doping gave positive S values and the $|S|$ value decreases monotonically with the σ values, clearly indicating that the carrier polarity is converted from n-type to p-type by the Ca and Cu doping.

Figure 5(b) shows the temperature dependence of σ for the most conductive samples of undoped, Ca-doped, and Cu-doped LaMnPO. The σ value of 10 at. % Cu doped LaMnPO reaches ~ 1 S cm^{-1} at RT and larger than that of the Ca doped LaMnPO, suggesting the Cu doping is more effective than the Ca doping to achieve better p-type conductivity. The σ values of all the samples exhibit thermally activated behaviors, and the apparent activation energies (E_a) are 0.06 eV for Cu 10 at. % doped LaMnPO, 0.08 eV for Cu 5 at. % doped LaMnPO, 0.21 eV for the Ca 7 at. % doped LaMnPO, 0.24 eV for the Ca 5 at. % doped LaMnPO, and 0.29 eV for the undoped LaMnPO. These can be explained with a simple semiconductor model. If the E_a values are assumed to reflect the Fermi level measured from the band edges (E_F) and the drift mobilities (μ) of the electron and hole are ~ 1 cm^2/Vs, these conductivities and the E_a values are explained with a constant value of the effective density of states $N_{\text{eff}} \sim 4.5 \times 10^{19}$ cm^{-3} using the equations $\sigma = en\mu$ and $n = N_{\text{eff}} \exp(-E_F/k_BT)$, where e is the elementary electric charge, n is the free carrier density, and k_B is the Boltzmann constant. This strongly suggests that the carriers flow by band conduction. As a result, LaMnPO is concluded to be a bipolar semiconductor.

Figure 6 shows mass magnetic susceptibility (χ_g) as a function of temperature from 375 to 2.5 K. The χ_g value at 300 K is very small at only 2.9×10^{-6} emu/g, and gradually decreases as the temperature decreases from 375 to 150 K. The small χ_g is not explained by ferromagnetism, and the small positive slope of the $\chi_g - T$ plot suggests that a phase

transition occurs at a higher temperature. Along with the result of the neutron diffraction Rietveld analysis, an AFM spin ordering is concluded to occur in this higher temperature range. Similar results are reported for BaMnPF, whose crystal structure is the same as LaMnPO except that the La–O insulating layer is replaced with the Ba–F layer.[37] It would also be worth comparing with $BaMn_2P_2$ with the $ThCr_2Si_2$ structure, which is composed of similar Mn–P layers and Ba layers.[38] $BaMn_2P_2$ exhibits similar electronic and magnetic properties; i.e., it is an AFM semiconductor with the Néel temperature >750 K. The spin configuration in the Mn–P layer is the same as that in LaMnPO. On the other hand, the interlayer spin coupling in $BaMn_2P_2$ is antiparallel and different from that in LaMnPO (parallel). It indicates that significant magnetic interaction exists between the Mn–P layers in $BaMn_2P_2$, although the interlayer distance is rather large at 0.65 nm. While, the present neutron diffraction study for LaMnPO did not exhibit a *c*-axis superlattice diffraction, which must be observed if the interlayer spin coupling is of antiparallel. We, therefore, concluded that the interlayer spin coupling is of parallel, but we like to note that the same result is obtained for the case that the spins are not ordered between the Mn–P layers. We consider that the latter case would also be reasonable because the larger interlayer distance in LaMnPO (0.88 nm) weakens the magnetic interaction. In addition, the spin moment of an Mn ion in $BaMn_2P_2$ is determined to be 4.2 μ_B/Mn by neutron diffraction at RT, which is rather larger than that in LaMnPO (2.26 μ_B/Mn), although the local coordination structures around the Mn ions are almost the same in $BaMn_2P_2$ and LaMnPO; i.e., the differences of the Mn–P distances and the P–Mn–P bonding angles are less than 1%. Furthermore, GGA+U calculations (details will be discussed later for LaMnPO) also gave almost the same spin moments for LaMnPO and $BaMn_2P_2$. We speculate that the observed smaller spin moment in LaMnPO suffers from the Larmor precession and reflects the projection of the total spin to the *c*-axis; while, the spin moments in $BaMn_2P_2$ is close to the full moment of high-spin configuration Mn^{2+} ion (5 μ_B) and the precession effect would be negligible.

On the other hand, χ_g starts increasing as the temperature decreases at <150 K. The increase in the low-temperature region seems to follow the Curie–Weiss law (CW), and the effective magnetic moment estimated from the CW curve is in the order of 0.1 μ_B/formula unit (f.u.). Because the high-power XRD measurements verified the impurity phase was less than 0.1%, the increase is not simply attributed to paramagnetic crystalline impurities in the sample. Figure 6(b) shows the magnetic moment-magnetic field (*M-H*) curves at 300, 100, and 2 K. The observed magnetic moments (e.g., 1.3×10^{-2} μ_B/f.u. at 2 K at 50 000 Oe) are far below the values obtained by fitting the Brillouin function to both high and low spin configurations of a Mn^{2+} ion (4.9 μ_B/Mn and 0.93 μ_B/Mn, respectively), which is also consistent with the AFM ordering. The *M-H* curves show very small but finite hystereses below 100 K, displayed in the inset of Fig. 6(b). The spontaneous magnetic moment is estimated from the extrapolation of the linear region (>30 000 Oe) in the *M-H* curve and is 0.004 μ_B/f.u. at 2 K. If the spontaneous magnetic moment comes from Mn ions in an impurity phase, it should correspond to an impurity fraction >0.4%. However, because our XRD measurements have a detection limit of ~0.1%, this magnetic moment value is hardly attributable to a crystalline FM impurity. Another possible explanation is that the hystereses in the *M-H* curves and the sharp increase in χ_g at <150 K come from a magnetic phase transition from the antiferromagnetism to a weak ferromagnetism. However, further experiments are required to make a final conclusion.

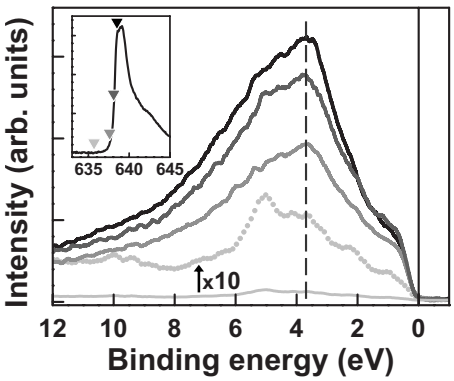

FIG. 7. RPES spectra at the excitation photon energies from 636 eV (off-resonant energy) to 639 eV (on-resonant). The off-resonant spectrum at bottom is magnified by a factor of 10 at the second bottom spectrum. Inset shows the XAS spectra at the Mn L_3 edge and the excitation energy positions (triangles) at which the PES spectra were measured. The dashed vertical line indicates the maximum peak position (3.7 eV) in the on-resonant spectra.

C. Electronic structures

Figure 7 shows the PES spectra of the Ca-doped *p*-type LaMnPO measured with excitation photon energies near the Mn L_3 edge. The energy is measured from the Fermi level. In the off-resonant spectrum, the clear signals appear at binding energies below ~0.1 eV, which correspond to the valence band maximum (VBM), and the valence band width is estimated to be ~6 eV. It turns out that the Fermi level is ~0.1 eV above the VBM, which is consistent with the *p*-type conduction of this sample. To distinguish the contribution of the Mn 3*d* orbitals, resonant photoemission spectra at the Mn L_3 edge are also shown in Fig. 7. Besides the main peak of the on-resonant spectra at 3.7 eV, almost all the valence band regions are enhanced by increasing the excitation photon energy from 636 to 639 eV, indicating that Mn 3*d* orbitals largely contribute to the band near 3.7 eV, but also spread over the valence band as well.

Figure 8 shows the total density of states (TDOS) obtained by the GGA+U calculations with U_{eff} parameters varied from 0 to 4 eV, along with the projected densities of two spin states (denoted α and β states, respectively) in Mn 3*d*. The RPES spectrum is also shown in the top panel for comparison. LaMnPO is found to be highly spin-polarized even for small $U_{\text{eff}}\leq1$ eV, while the larger U_{eff} correspond to almost completely spin-polarized states. The spin moment of a Mn ion is 3.25 μ_B for $U_{\text{eff}}=0$ eV and increased to >4 μ_B for $U_{\text{eff}}\geq2$ eV. The latter value is close to the full magnetic moment of the high-spin configuration for Mn $(3d_{\text{up}})^5$. A

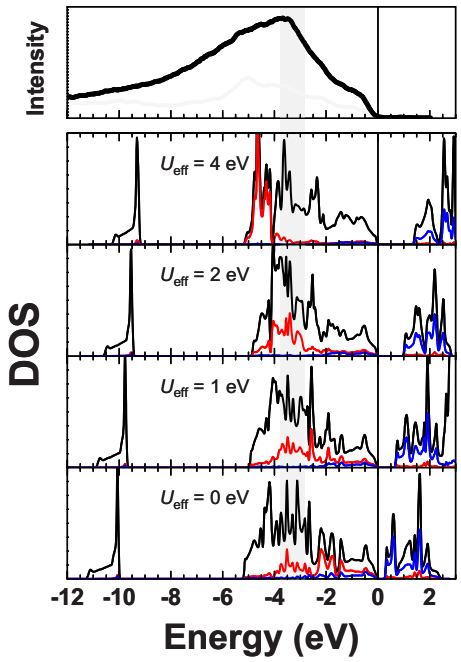

FIG. 8. (Color online) TDOS (black line) along with projected densities of α (red line) and β spin states (blue line) in Mn 3*d* obtained by GGA+U calculations with the AFM configuration obtained by the neutron Rietveld analysis [Fig. 3(c)]. The U_{eff} parameters were varied from 0 to 4 eV. The black line and the light gray dotted line in the top panel show the on-resonant and the magnified off-resonant PES spectra, respectively.

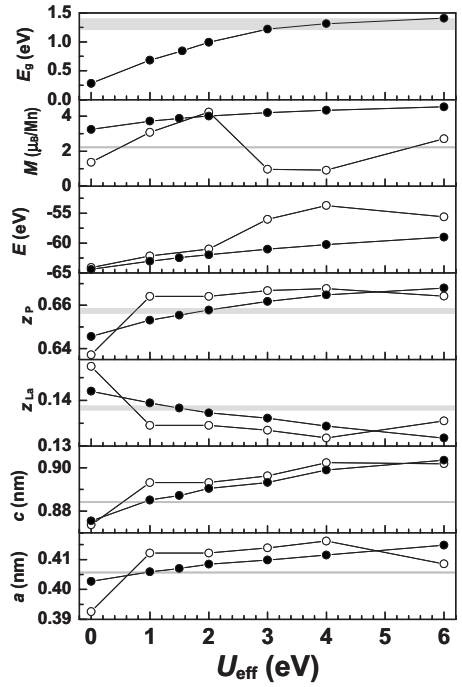

FIG. 9. Crystal structure parameters (the lattice parameters *a* and *c*, the *z* coordinates of the La and P ions), total energies (*E*), spin moments (*M*), and band gaps (E_g) obtained by the structure relaxation calculations by the GGA+U calculations for the FM (open circles) and AFM (closed circles) configurations. The gray horizontal lines and shadowed areas indicate the ranges of the experimental values.

plausible U_{eff} parameter would be determined based on the experimental results such as the RPES spectrum, the crystal structure, and the optical band gap. The energy positions of the calculated Mn 3*d* main peaks are deeper than 4 eV from the Fermi energy for $U_{eff} \geq 4$ eV, which do not correspond to the RPES result where the main resonant peak is located at ~3.7 eV. Figure 9 summarizes the parameters of the optimized crystal structures (the lattice parameters *a* and *c*, and the *z* coordinates of the La and P ions), the total energies (*E*), the spin moments (*M*) of the Mn ion, and the band gaps (E_g) obtained from the GGA+U calculations for the FM and AFM configurations plotted against the U_{eff} value. The gray horizontal lines and shadowed areas indicate the ranges of the experimental values. They suggest that the experimental optical band gap (~1.3 eV) is reproduced reasonably when U_{eff}=3–4 eV. The magnetic moment value obtained by the neutron Rietveld analysis (2.26 μ_B) is much smaller than all the values obtained by the GGA+U calculations, but those from U_{eff}=0–1.5 eV (3.25–3.8 μ_B in the AFM phase) are reasonably close to the experimental values compared with the others obtained for the larger U_{eff} values. All the crystal structure parameters are reproduced well with the U_{eff} values of 1–2 eV. The total energy values indicate that the AFM phase is more stable than the FM phase, which is consistent with the experimental result of the AFM phase at RT. Considering these results, the U_{eff} parameter of 1.5 eV is considered to be the safest value at present. Figure 10(a) shows the projected density of states (PDOS) decomposed to the respective ions and Mn 3*d* spin states. The Mn 3*d* and P 3*p* orbitals spread to almost all the valence band region and the conduction band region, while the O 2*p* orbitals are concentrated in the deep valence band region at −2 to −4 eV. The VBM and the conduction band minimum (CBM), which correspond to the transport paths of holes and electrons, respectively, are composed mainly of the Mn 3*d*-P 3*p* hybridized orbitals. This feature is similar to a superconductor in the family compounds, LaFePO, in the aspect that the Fermi level is composed mainly of Fe 3*d*; but it should be noted that the contribution of P 3*p* orbitals is much smaller for LaFePO. The indirect transition at the absorption edge observed in Fig. 4 is supported by the band energy diagram in Fig. 10(b). The VBM is located at the Γ point while the CBM at the *M* point. Another interesting feature is found in the anisotropy of the VBM band dispersions; the band dispersion along the Γ−*Z* direction is much smaller than that along the Γ−*X* direction, which suggests a strong two-dimensional nature for the electronic structure similar to LaCu*Ch*O (Ref. 30) and La*MX*O (*M*=Fe, Ni).[4–6]

IV. SUMMARY

Electrical and optical measurements clarified that LaMnPO is a bipolar semiconductor with an indirect band gap energy of ~1.3 eV. The AFM ordering structure was observed by the magnetic and the neutron diffraction measurements. Neutron diffraction analyses revealed that the spin configuration in LaMnPO is of antiparallel in the Mn–P plane while of parallel between the Mn–P planes. The magnetic moment was estimated to be 2.26 μ_B/Mn from the neutron diffraction analysis.

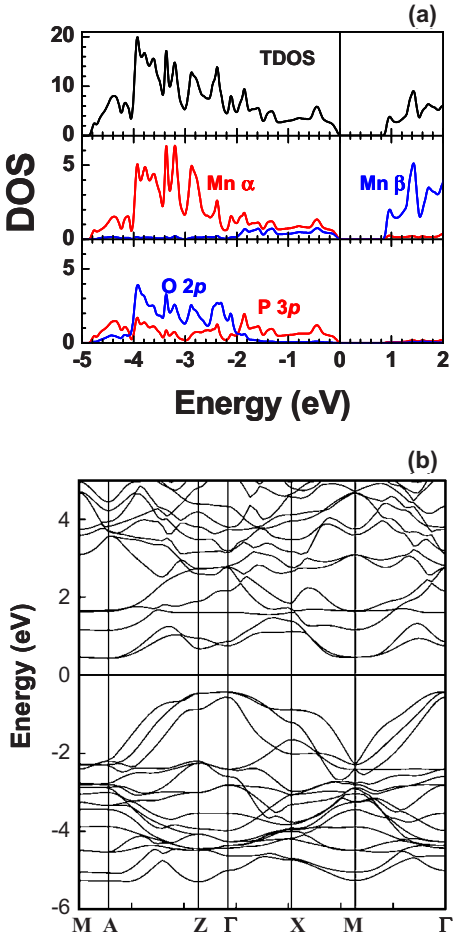

FIG. 10. (Color online) (a) Total and PDOSs for Mn $3d$ (α and β spin states), P $3p$, and O $2p$ orbitals calculated with U_{eff}=1.5 eV for Mn $3d$ electrons using the AFM configuration obtained by the neutron Rietveld analysis [Fig. 3(c)]. (b) Calculated band structure of LaMnPO with the AFM configuration. The energy is measured from the Fermi energy.

ACKNOWLEDGMENTS

We are indebted to Dr. N. Igawa (JAEA) for his help in the neutron diffraction measurement, to Dr. Yuji Saitoh and Dr. Shin-ichi Fujimori (JAEA) for their help in the resonant photoemission spectroscopy measurements, and to Dr. H. Hiramatsu (ERATO-SORST, JST) for his help with the measurements and his valuable discussions. The synchrotron radiation experiment was performed under the Common-Use Facility Program of JAEA (Proposal No. 2006B-E22).

[1]J. G. Bednorz and K. A. Muller, Z. Phys. B **64**, 189 (1986).
[2]T. Kimura, Y. Tomioka, H. Kuwahara, A. Asamitsu, M. Tamura, and Y. Tokura, Science **274**, 1698 (1996).
[3]I. Terasaki, Y. Sasago, and K. Uchinokura, Phys. Rev. B **56**, R12685 (1997).
[4]S. Lebègue, Phys. Rev. B **75**, 035110 (2007).
[5]W. B. Zhang, X. B. Xiao, W. Y. Yu, N. Wang, and B. Y. Tang, Phys. Rev. B **77**, 214513 (2008).
[6]D. J. Singh and M.-H. Du, Phys. Rev. Lett. **100**, 237003 (2008).
[7]Y. Kamihara, H. Hiramatsu, M. Hirano, R. Kawamura, H. Yanagi, T. Kamiya, and H. Hosono, J. Am. Chem. Soc. **128**, 10012 (2006).
[8]T. Watanabe, H. Yanagi, T. Kamiya, Y. Kamihara, H. Hiramatsu, M. Hirano, and H. Hosono, Inorg. Chem. **46**, 7719 (2007).
[9]Y. Kamihara, T. Watanabe, M. Hirano, and H. Hosono, J. Am. Chem. Soc. **130**, 3296 (2008).
[10]H. Takahashi, K. Igawa, K. Arii, Y. Kamihara, M. Hirano, and H. Hosono, Nature (London) **453**, 376 (2008).
[11]G. F. Chen, Z. Li, D. Wu, G. Li, W. Z. Hu, J. Dong, P. Zheng, J. L. Luo, and N. L. Wang, Phys. Rev. Lett. **100**, 247002 (2008).
[12]Z. A. Ren, J. Yang, W. Lu, W. Yi, G. C. Che, X. L. Dong, L. L. Sun, and Z. X. Zhao, Mater. Res. Innovations **12**, 105 (2008).
[13]Z. A. Ren, J. Yang, W. Lu, W. Yi, X. L. Shen, Z. C. Li, G. C. Che, X. L. Dong, L. L. Sun, F. Zhou, and Z. X. Zhao, Europhys. Lett. **82**, 57002 (2008).
[14]Z. A. Ren, W. Lu, J. Yang, W. Yi, X. L. Shen, C. Zheng, G. C. Che, X. L. Dong, L. L. Sun, F. Zhou, and Z. X. Zhao, Chin. Phys. Lett. **25**, 2215 (2008).
[15]P. Cheng, L. Fang, H. Yang, X. Zhu, G. Mu, H. Luo, Z. Wang, and H. H. Wen, Sci. China, Ser. G **51**, 719 (2008).
[16]H. Yanagi, R. Kawamura, T. Kamiya, Y. Kamihara, M. Hirano, T. Nakamura, H. Osawa, and H. Hosono, Phys. Rev. B **77**, 224431 (2008).
[17]K. Kayanuma, H. Hiramatsu, M. Hirano, R. Kawamura, H. Yanagi, T. Kamiya, and H. Hosono, Phys. Rev. B **76**, 195325 (2007).
[18]Y. Takano, S. Komatsuzaki, H. Komasaki, T. Watanabe, Y. Takahashi, and K. Takasem, J. Alloys Compd. **451**, 467 (2008).
[19]A. T. Nientiedt, W. Jeitschko, P. G. Pollmeier and M. Brylak, Z. Naturforsch. **52B**, 560 (1997).
[20]T. Watanabe, H. Yanagi, Y. Kamihara, T. Kamiya, M. Hirano, and H. Hosono, J. Solid State Chem. **181**, 2117 (2008).
[21]T. Mine, H. Yanagi, T. Kamiya, Y. Kamihara, M. Hirano, and H. Hosono, Solid State Commun. **147**, 111 (2008).
[22]X-ray photoemission spectroscopy measurements revealed that the valence state of doped Cu ion was not divalent (Cu^{2+}) but monovalent (Cu^{+}).
[23]Bruker AXS. TOPAS, version 3, Bruker AXS, Karlsruhe, Germany, 2005.
[24]F. Izumi and T. Ikeda, Mater. Sci. Forum **321-324**, 198 (2000).
[25]K. Kayanuma, H. Hiramatsu, T. Kamiya, M. Hirano, and H. Hosono, J. Appl. Phys. **105**, 073903 (2009).
[26]G. Kresse and J. Furthmuller, Phys. Rev. B **54**, 11169 (1996).
[27]P. E. Blöchl, Phys. Rev. B **50**, 17953 (1994).
[28]G. Kresse and D. Joubert, Phys. Rev. B **59**, 1758 (1999).
[29]S. L. Dudarev, G. A. Botton, S. Y. Savrasov, C. J. Humphreys, and A. P. Sutton, Phys. Rev. B **57**, 1505 (1998).
[30]K. Ueda, H. Hiramatsu, H. Ohta, M. Hirano, T. Kamiya, and H. Hosono, Phys. Rev. B **69**, 155305 (2004).
[31]B. I. Zimmer, W. Jeitschko, J. H. Albering, R. Glaum, and M. Reehuis, J. Alloys Compd. **229**, 238 (1995).
[32]A. T. Nientiedt and W. Jeitschko, Inorg. Chem. **37**, 386 (1998).
[33]C. de la Cruz, Q. Huang, J. W. Lynn, J. Li, W. Ratcliff, J. L. Zarestky, H. A. Mook, G. F. Chen, J. L. Luo, N. L. Wang, and P. Dai, Nature (London) **453**, 899 (2008).
[34]P. Kubelka and F. Munk, Z. Tech. Phys. (Leipzig) **12**, 593 (1931).
[35]P. Kubelka, J. Opt. Soc. Am. **38**, 448 (1948).
[36]H. Hiramatsu, K. Ueda, H. Ohta, M. Hirano, M. Kikuchi, H. Yanagi, T. Kamiya, and H. Hosono, Appl. Phys. Lett. **91**, 012104 (2007).
[37]H. Kabbour, L. Cario, and F. Boucher, J. Mater. Chem. **15**, 3525 (2005).
[38]S. L. Brock, J. E. Greedan, and S. M. Kauzlarich, J. Solid State Chem. **113**, 303 (1994).